Suspended sediment and hydrodynamics above mildly sloped long wave ripples

Yeon S. Chang

Meteorology and Physical Oceanography, Rosenstiel School of Marine and Atmospheric Science, University of Miami, Miami, Florida, USA

Daniel M. Hanes[1]

Coastal and Marine Geology, U.S. Geological Survey Pacific Science Center, Santa Cruz, California, USA

[1]   We investigate the spatial and temporal distribution of suspended sediment and the associated hydrodynamics over mildly sloped long wave ripples on the inner shelf. These bedforms had wavelengths of approximately 1 m and heights of approximately 5 cm, in a mean water depth of 4 m. The vertical and temporal structures of the suspended sediment concentration (SSC) are consistent with the entrainment of sediment on the offshore flank of the ripple, and rapid vertical mixing at the time of flow reversal, followed by advection onshore by the onshore fluid motion. This work confirms that the mechanism for sediment suspension above low-amplitude, long wave ripples is similar to the vortex formation process expected over steeper vortex ripples. Numerical simulations of the flow using the Dune2d model indicate that a separated rotational flow structure is generated at the flank of the ripple on the seaward side of the ripple crest, near the time of flow reversal. The simulations indicate that only one vortex is formed during each wave period, in agreement with the field observations. This asymmetry is due mainly to the presence of an offshore mean near-bed current of approximately 6 to 8 cm/s. The SSC is calculated by the model and compared to the field observations. A hydraulic bed roughness of 10 to 15 median grain diameters (d_{50}) was used in order to match the model prediction to the observed SSC approximately 1 cm above the seabed (cab). However, the modeled SSC and turbulent kinetic energy were significantly lower than the field observations at elevations exceeding approximately 2 cab.   *INDEX TERMS:* 1815 Hydrology: Erosion and sedimentation; 3022 Marine Geology and Geophysics: Marine sediments—processes and transport; 3045 Marine Geology and Geophysics: Seafloor morphology and bottom photography; 4546 Oceanography: Physical: Nearshore processes; 4558 Oceanography: Physical: Sediment transport; *KEYWORDS:* bedform, ripple, seabed, suspended sediment

1.   Introduction

[2]   The distribution of the suspended sediment concentration (SSC) near the seabed under wave and current conditions is important to sediment transport in coastal areas. As waves propagate from deep water toward the shoreline, they shoal and refract across the continental shelf, and their height generally increases in the inner shelf and nearshore region until the waves break. During this process the waves and currents entrain sediment from the seabed into suspension. The shape of the local seabed strongly influences entrainment and suspension processes. Hydrodynamic conditions over a rippled seabed vary horizontally on the scale of the bedforms, but above a flat seabed, hydrodynamics are spatially uniform over these scales. Sediment suspension events therefore exhibit very different patterns above flat versus rippled beds [e.g., *Vincent et al.*, 1991; *Hay and Bowen*, 1994].

[3]   The distribution of SSC over various seabeds has been investigated for several decades. For example, *Bagnold* [1946] suggested that the sediments are entrained into a vortex that is formed at the lee of the ripple crest and the vortex is ejected upward as the flow reverses. He called these bedforms "vortex ripples." During the entrainment and suspension process, a large amount of sediment falls quickly to bed, but some of the sediment is carried with the vortex, forming a cloud of sediment. From an experiment carried out in an oscillatory flow water channel, *Sleath* [1982] confirmed the generation of a vortex and its influence on the temporal and spatial distributions of SSC over rippled beds.

---

[1]Also at Department of Civil and Coastal Engineering, University of Florida, Gainesville, Florida, USA.

Report Documentation Page	*Form Approved* *OMB No. 0704-0188*

Public reporting burden for the collection of information is estimated to average 1 hour per response, including the time for reviewing instructions, searching existing data sources, gathering and maintaining the data needed, and completing and reviewing the collection of information. Send comments regarding this burden estimate or any other aspect of this collection of information, including suggestions for reducing this burden, to Washington Headquarters Services, Directorate for Information Operations and Reports, 1215 Jefferson Davis Highway, Suite 1204, Arlington VA 22202-4302. Respondents should be aware that notwithstanding any other provision of law, no person shall be subject to a penalty for failing to comply with a collection of information if it does not display a currently valid OMB control number.

1. REPORT DATE **18 FEB 2004**	2. REPORT TYPE	3. DATES COVERED **00-00-2004 to 00-00-2004**
4. TITLE AND SUBTITLE **Suspended sediment and hydrodynamics above mildly sloped long wave ripples**		5a. CONTRACT NUMBER
		5b. GRANT NUMBER
		5c. PROGRAM ELEMENT NUMBER
6. AUTHOR(S)		5d. PROJECT NUMBER
		5e. TASK NUMBER
		5f. WORK UNIT NUMBER
7. PERFORMING ORGANIZATION NAME(S) AND ADDRESS(ES) **University of Miami,Meteorology and Physical Oceanography,Rosenstiel School of Marine and Atmospheric Science,Miami,FL,33176**		8. PERFORMING ORGANIZATION REPORT NUMBER
9. SPONSORING/MONITORING AGENCY NAME(S) AND ADDRESS(ES)		10. SPONSOR/MONITOR'S ACRONYM(S)
		11. SPONSOR/MONITOR'S REPORT NUMBER(S)
12. DISTRIBUTION/AVAILABILITY STATEMENT **Approved for public release; distribution unlimited**		
13. SUPPLEMENTARY NOTES		
14. ABSTRACT		
15. SUBJECT TERMS		

16. SECURITY CLASSIFICATION OF:			17. LIMITATION OF ABSTRACT **Same as Report (SAR)**	18. NUMBER OF PAGES **16**	19a. NAME OF RESPONSIBLE PERSON
a. REPORT **unclassified**	b. ABSTRACT **unclassified**	c. THIS PAGE **unclassified**			

Standard Form 298 (Rev. 8-98)
Prescribed by ANSI Std Z39-18

[4] Recently developed instrumentation has made quantitative field studies of these phenomena possible. Acoustic instruments for measuring the SSC such as the Acoustic Backscatter System (ABS) have enabled the measurement of nearly instantaneous concentration profiles [*Lee and Hanes*, 1995; *Osborne and Vincent*, 1996; *Thosteson and Hanes*, 1998]. The Multiple Transducer Array (MTA) has enabled the measurement of bedforms in one dimension [*Jette and Hanes*, 1997; *Hanes et al.*, 2001]. These and other acoustic instruments provide times series of fluid motions, SSC, and bedforms (see *Thorne and Hanes* [2002] for a summary). For example, through the analysis of the velocity and the SSC measured in the field, *Vincent et al.* [1999] showed that the suspended sediment distribution is consistent with vortex entrainment. They found that high sediment concentrations are located over the ripple trough at times of peak wave velocity.

[5] Sediment suspension and its distribution have also been investigated through various numerical models. Over a flat bed, *Fredsoe et al.* [1985] suggested a one-dimensional (1-D) time-dependent diffusion type model for suspended sediment distribution. In this model, they used the momentum integral method to derive a time-varying eddy viscosity that enabled the calculations of the time variation of the SSC. The instantaneous bed concentration was assumed to be a function of bed shear stress, resulting in the maximum bed concentration at the time of maximum fluid velocity. Time lags were found for the peak concentration at different elevations due to the diffusion processes. Another one-dimensional description of suspended sediment distribution is a convection-diffusion type model [*Nielsen*, 1988, 1991, 1992a, 1992b]. By introducing a "pickup" function that describes the instantaneous pickup rate at the bed, the model accounts for the large-scale mixing (convection) as well as small-scale mixing (diffusion). *Lee and Hanes* [1996] also suggested a one-dimensional, convection-diffusion type model that combined the eddy diffusivity of Wikramanayake [*Wikramanayake*, 1993; *Grant and Madsen*, 1979] and Nielsen's pickup function.

[6] The time-dependent flow due to waves over ripples beds has also been studied numerically. Recently, *Barr et al.* [2004] applied a 3-D DNS model to investigate flow over various shaped ripples with typical slopes of 0.1 to 0.2. Their results confirmed the previous paradigm that flow separation near the ripple crest results in organized flow structures that are ejected upward by the reversing flow. Several models are also available for investigations of 2-D, time-dependent hydrodynamics and suspended sediment distributions over rippled seabeds [*Hansen et al.*, 1994; *Black et al.*, 1997; *Andersen*, 1999]. The Dune2d numerical model is a boundary layer numerical model that calculates hydrodynamics and sediment concentration fields above rippled seabeds [*Tjerry*, 1995; *Andersen*, 1999]. It resolves the turbulent vortices around the ripples by using any of several turbulence closure models. We will use the Dune2d numerical model to describe the detailed hydrodynamics and sediment dynamics due to the waves and currents over realistic bedforms. The model allows for calculation of flow details that were not possible to measure directly in the field, such as vortex formation.

[7] The purpose of this paper is to investigate the suspended sediment distributions over gently sloped long wave
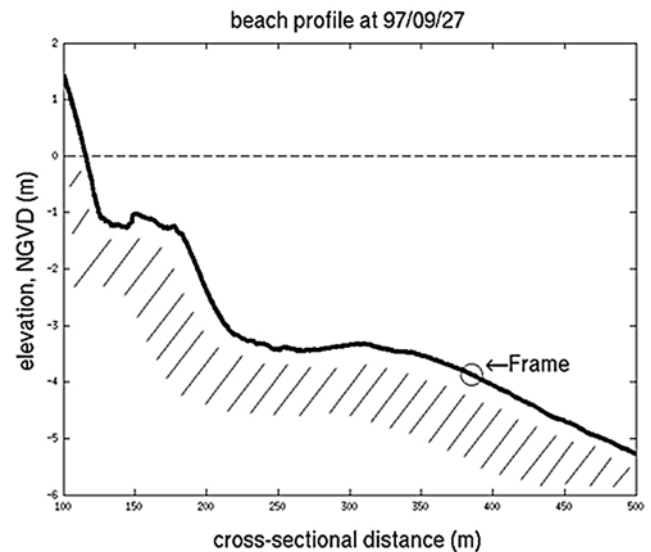
Figure 1. Beach profile and the location of the instruments; data are provided by U.S. Army Corps of Engineering Field Research Facility.

ripples (LWR) through the analysis of the measured field data, and through a numerical study using Dune2d. The study is focused on examining the hypothesis that flow separation over LWR causes the entrainment and transport of suspended sediment. The model predictions are compared with the field measurements, and both are utilized to describe the details of the hydrodynamics that cause sediment suspension.

2. Field Experiment Overview and Analysis Technique

[8] The data to be presented were collected during a field experiment that was conducted to investigate small-scale sediment dynamics near the seabed in the nearshore and inner shelf regions. Our efforts were part of the broader based SandyDuck'97 experiment, carried out at the U.S. Army Corps of Engineering Field Research Facility (FRF), in Duck, North Carolina. The experiment lasted for approximately 8 weeks from September to November 1997 [*Hanes et al.*, 1998]. Our array of instrumentation was deployed in approximately 4 m depth, which was usually outside the surf zone. The cross-shore bed slope averaged over several meters near the instrument array was approximately 0.01 (Figure 1), and the median sand diameter of the surficial sediments was 0.16 mm.

[9] The instruments measured the local hydrodynamics using a pressure sensor and two Sontek Acoustic Doppler Velocimeters (ADV). The SSC was measured with a three-frequency ABS that was custom built by the Ministry of Agriculture, Fisheries, and Food in the U.K. The local bedforms were measured with a Seatek MTA in one dimension over 2.5 m with a sampling interval of either 2 or 3 s. The sampling frequency of the other instruments ranged from 1 to 4 Hz. A schematic of the instrumentation is shown in Figure 2.

[10] For the present study, two data sets with similar hydrodynamic conditions are chosen. In each case the
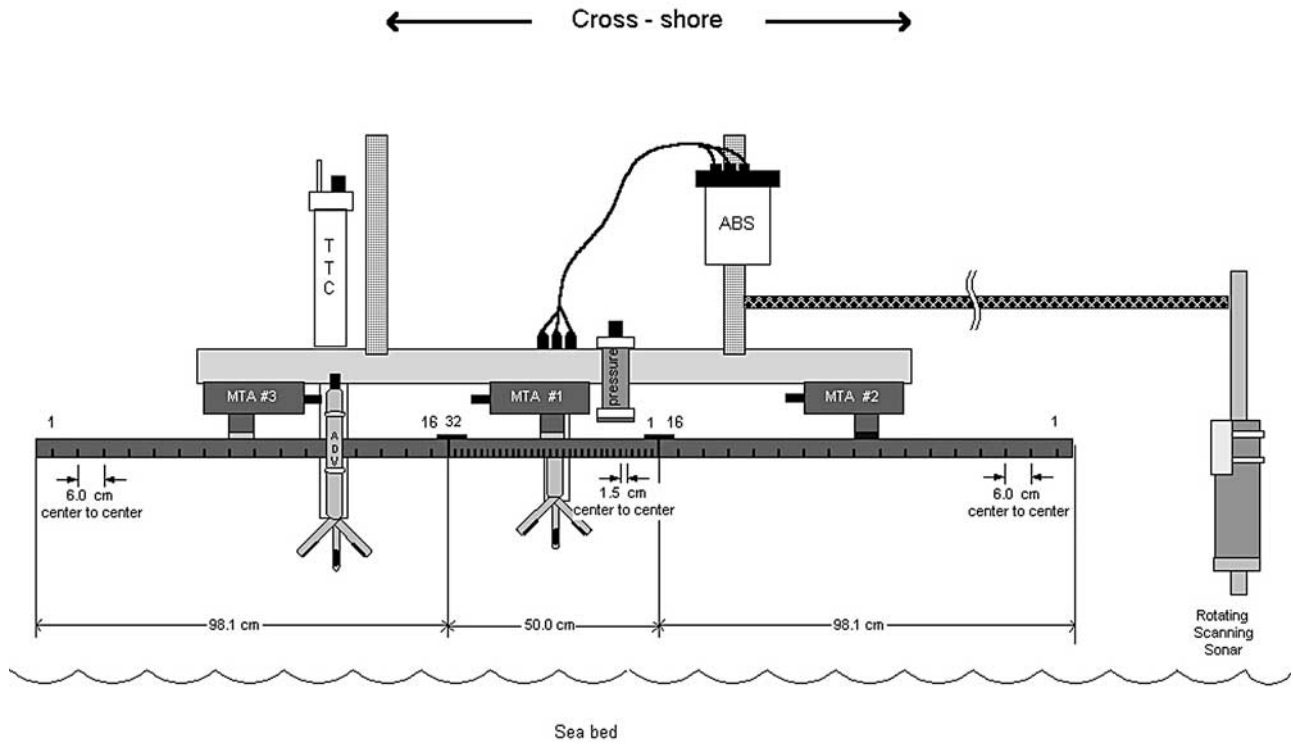
Figure 2. Instrumentation schematic at SandyDuck'97 field experiment.

seabed exhibited LWR that are typical of the location [*Hanes et al.*, 2001]. In these two data sets, however, the ABS was at relatively different locations on the ripple profile. The bedforms and the locations of ADV and ABS measurements are shown in Figure 3. The two different bedform conditions are denoted by case A and case B. In case A, "P1" indicates the ADV measurement volume, located near the ripple crest and approximately 22 cm above the bed (cab). "P2" in case B indicates the ADV measurement volume, located above the offshore slope of the ripple crest approximately 23 cab. The times of the measurements are 11 pm on 25 October 1997 for case A and 5 pm on 27 September 1997 for case B. Each bedform profile in Figure 3 is determined from the time average of a 30-min run. In case A, the seabed is covered by a LWR with about 0.9 m length and 0.06 m height. Case B has a similarly shaped ripple with length of 1.1 m and height of 0.05 m. Because the seabed profiles shown in Figure 3 have been averaged over 30 min, they have relatively smooth surfaces. However, individual bed profiles frequently have small wave ripples (SWR) superimposed on the LWR. The effects of superimposed ripples will be examined later in this work.

[11] The significant wave heights (H_{m0}) are similar for case A, 1.09 m, and case B, 1.12 m. Both wave spectra (Figure 4) show bimodal shapes, with peaks at frequencies of 0.13 Hz and 0.22 Hz. The local water depths are 4.1 m and 4.6 m for cases A and B, respectively, and the measurements were taken well outside the surf zone in both cases. The peak wave directions are 92.3° in case A and 87.7° in case B, where 90° is normal to the coastline. One of the important assumptions in the 2-D model to be used later is that the ripples observed in case A and case B are relatively uniform in the alongshore direction. The observations that the wave directions are normal to the coastline and that

there were no significant longshore currents both support this assumption, although we cannot completely rule out the possibility of 3-D ripple patterns. One interesting feature of the hydrodynamic conditions is that offshore mean flows
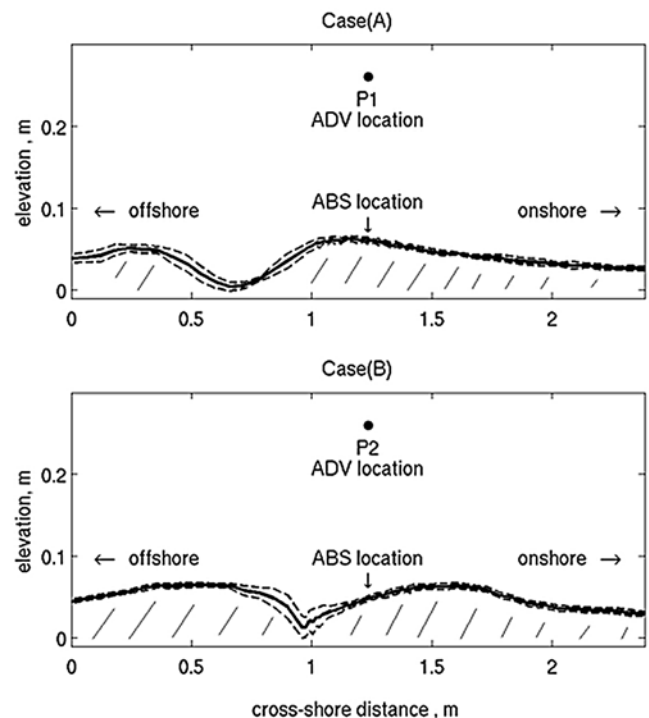
Figure 3. Time average and ±1 standard deviation of seabed location over 30 min, with instrument measurement locations.
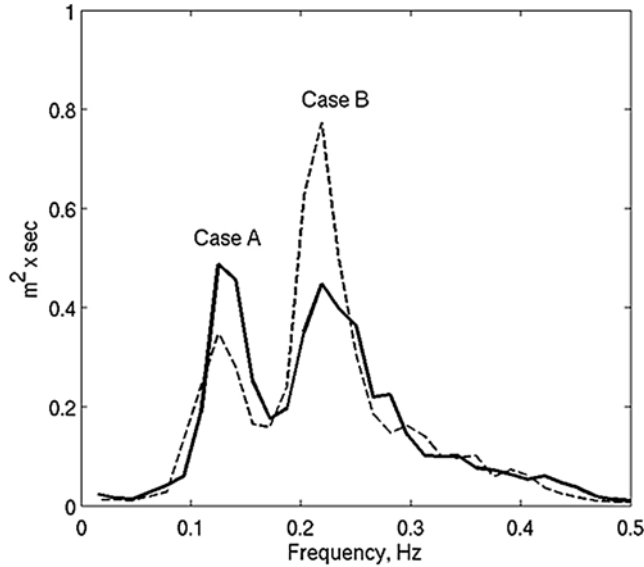
Figure 4. Comparison of the surface elevation spectrum: solid line, case A; dashed line, case B.

are observed in both cases. The magnitudes of the mean flow in offshore direction are 8.3 cm/s for case A and 6.1 cm/s for case B. The larger-scale circulation patterns that resulted in offshore mean flows near the seabed are not known. Whatever their origin, these mean flows had a strong influence upon the SSC temporal fluctuations, as will be seen in later sections. The overall hydrodynamic forcing conditions in both cases are similar, so we presume that the main differences observed in the SSC patterns between the two cases are related to the location of the sediment concentration measurements relative to the ripple profiles.

3. Model Overview and Forcing Conditions

[12] The Dune2d numerical model used was developed at the Technical University of Denmark [*Tjerry*, 1995; *Andersen*, 1999]. Dune2d is a 2-D boundary layer model composed of three modules: the mean flow, turbulence, and sediment transport modules. Reynolds averaged Navier-Stokes equations are employed for the flow module

$$\frac{\partial U_i}{\partial t} + U_j \frac{\partial U_i}{\partial x_j} = -\frac{1}{\rho}\frac{\partial P}{\partial x_i} + \frac{\partial}{\partial x_j}\left(2\nu S_{ij} - \tau_{ij}\right)$$
$$\frac{\partial U_i}{\partial x_i} = 0, \tag{1}$$

where the Reynolds stresses are expressed in terms of the Boussinesq approximation.

$$\tau_{ij} = 2\nu_t S_{ij} - \frac{2}{3}k\delta_{ij}. \tag{2}$$

[13] Closure is achieved using an eddy viscosity calculated from a turbulence closure model. Out of numerous possible models, we use the $K - \omega$ model that was developed by *Wilcox* [1998] in Dune2d because the $K - \omega$

model has been applied with success in areas with strong adverse pressure gradients [*Andersen*, 1999].

$$\frac{\partial k}{\partial t} + U_j \frac{\partial k}{\partial x_j} = \frac{\partial}{\partial x_j}\left[(\nu + \sigma^*\nu_t)\frac{\partial k}{\partial x_j}\right] - \overline{u_i u_j}\frac{\partial U_i}{\partial x_j} - \beta^* k\omega$$
$$\frac{\partial \omega}{\partial t} + U_j \frac{\partial \omega}{\partial x_j} = \frac{\partial}{\partial x_j}\left[(\nu + \sigma\nu_t)\frac{\partial \omega}{\partial x_j}\right] + \gamma\frac{\omega}{k}\left(-\overline{u_i u_j}\frac{\partial U_i}{\partial x_j}\right) - \beta\omega^2.$$
$$\tag{3}$$

[14] In equation (3), ω has the dimensions of reciprocal time, and can be interpreted as a frequency of the turbulent fluctuations. The closure coefficients given by *Wilcox* [1998] are used in the present work without any change in their values.

[15] Bottom, surface, and lateral boundary conditions are required for the model. At the bottom, a no-slip condition is applied for the flow, and the turbulent kinetic energy (TKE) is assumed to be zero. ω is specified at the bottom as a function of the friction velocity and hydraulic roughness. The domain upper surface is not allowed to change its shape (rigid lid), and the variables are assigned zero flux there. For the lateral boundary condition a cyclic condition is applied by linking the lateral boundaries such that the solution is periodic.

[16] The sediment transport calculations utilize the Engelund-Fredsoe formula [*Engelund and Fredsoe*, 1976] to determine the reference concentration. The bottom boundary condition for concentration is applied at the reference level, $y = 2d_{50}$ where d_{50} is the median grain diameter. The suspended sediment is modeled by the 2-D advection-diffusion equation

$$\frac{\partial C}{\partial t} + \frac{\partial UC}{\partial x} + \frac{\partial VC}{\partial y} = \frac{\partial w_s C}{\partial y} + \frac{\partial}{\partial x}\left(\varepsilon_s\frac{\partial C}{\partial x}\right) + \frac{\partial}{\partial y}\left(\varepsilon_s\frac{\partial C}{\partial y}\right), \quad (4)$$

where C is the suspended sediment concentration by volume, w_s is the settling velocity, ε_s is the sediment diffusivity that is assumed to be equal to eddy viscosity, and (U, V) are the fluid horizontal and vertical velocities. At the bottom, the reference concentration is determined from the local shear stress as a function of position and time.

[17] The governing equations are discretized implicitly in time using the Finite Volume method [*Patankar*, 1980] and written in general curvilinear coordinates to allow the grid to fit smoothly to the boundaries [*Tjerry*, 1995]. The pressure is nonhydrostatic, and there is no explicit equation for pressure; the PISO algorithm is used to find the pressure field [*Patankar*, 1980]. In order to avoid numerical diffusion, the ISNAS scheme that gives third-order accuracy is used for the discretization [*Zijlema*, 1996]. For detailed information on the discretization, readers are referred to *Tjerry* [1995] and *Patankar* [1980].

[18] For a given bedform such as the one used in this study, a grid system is generated using the hyperbolic grid generator with a high density of grid points near the bed. Following the advice of *Andersen* [1999] as well as our own sensitivity studies, a grid with 120 points in the horizontal and 60 points in the vertical was chosen to adequately resolve the flow. Figure 5 shows the grids for both cases. In order to apply the cyclic condition to the lateral boundaries, the bed elevations at the left and right boundaries are
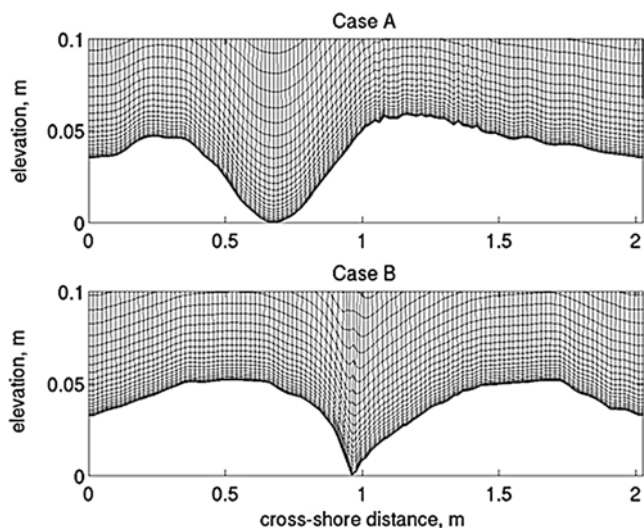
Figure 5. Computational grids used for the model simulations for (top) case A and (bottom) case B.

slightly modified to be equal after the physical domain has been resized from 0 to 2 m.

[19] Because all the model equations are dimensionless, the inputs to the model need to be parameterized with appropriate nondimensional values, such as Reynolds number, Froude number, and angular frequency. Those parameters can be estimated from the dimensional values, such as depth of domain (D), wave period (T), and maximum velocity (U_0) outside the boundary layer. In this study, D is chosen to be 1 m in order to give a sufficiently dense vertical grid. The wave period and the maximum velocity used to force the model are determined based on the field measurements. The wave period is 6.0 s and U_0 is 0.40 m/s for case A. For case B, the wave period is 6.5 s and U_0 is 0.39 m/s. The median grain size is 0.16 mm. From these values, the nondimensional parameters are found as

$$\text{DWF} = D/a = \frac{2\pi D}{U_0 T} = 2.62 \text{(case A)}, 2.48 \text{ (case B)}$$

$$\text{RN} = \frac{U_0 D}{\nu} = 4.0 \times 10^5 \text{ (case A)}, 3.9 \times 10^5 \text{(case B)}$$

$$\text{FN} = \frac{U_0}{\sqrt{gD}} = 0.128 \text{(case A)}, 0.125 \text{(case B)},$$

where DWF is dimensionless wave frequency, RN is Reynolds number, and FN is Froude number.

[20] The bed roughness (K_N) for a flat bed is often chosen to be 2.5 times the median grain diameter. However, when ripples are present, their dimensions represent another scale of hydraulic roughness. Other choices for roughness can also be found in the literature, so it is not clear what roughness is truly appropriate to use as a boundary condition for this model. The use of $2.5d_{50}$ tends to underestimate the model-predicted concentrations when compared with the measurements. A hydraulic roughness based on the dimension of small wave ripples using the formula of

Nielsen [1992a] results in a value of approximately $17d_{50}$, which is more than an order of magnitude larger than the flat sand bed value. We found through iterations that a roughness of approximately $10.5d_{50}$ resulted in a mean model-predicted concentration in agreement with the measurement at the lowest elevation (1.17 cab) for case A and $14.0d_{50}$ for case B, so we chose to use these values for the simulations. We recognize that this choice is somewhat arbitrary; we use this grudgingly until a better formulation or understanding becomes available. Using this nondimensional roughness, K_N/D was then set to be 1.65×10^{-3} for case A and 2.19×10^{-3} for case B. In order to get a stable solution, at least four wave periods are needed. Each wave cycle is divided into 240 time steps, which gives the nondimensional time step, $\Delta t = \frac{2\pi}{240}$rad.

4. Results

4.1. Observed Suspension Patterns

[21] In the nearshore environment the suspension of sand is generally intermittent and tends to occur more often during relatively larger waves and during wave groups [*Brenninkmeyer*, 1976; *Thornton and Morris*, 1978; *Hanes*, 1988, 1991]. This is true for the present observations, as seen in Figure 6, which shows a time series of SSC. For this reason it is useful to isolate times of high SSC in order to investigate the dynamic processes leading to suspension. A common approach has been to select and ensemble average suspension events in order to obtain a description of a typical suspension event. One way of ensemble averaging is by wave phase [*Osborne and Vincent*, 1996; *Vincent et al.*, 1999]. The advantage of this technique is that the temporal variation of the concentration distribution may be compared with the flow at each wave phase. However, because the concentration events only occur intermittently in the field,
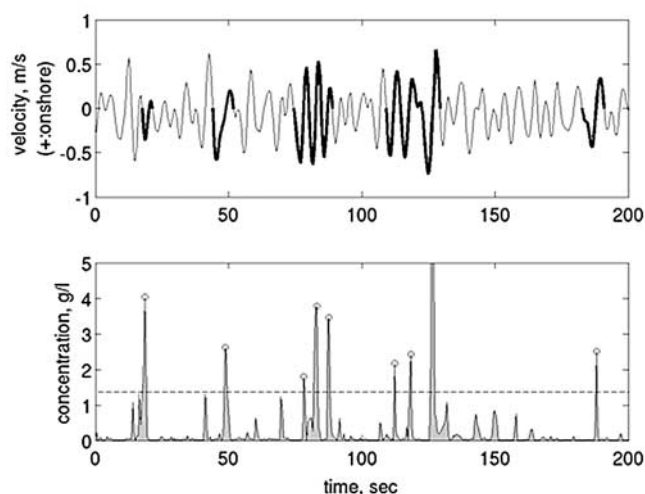
Figure 6. Time series of (top) cross-shore horizontal velocities and (bottom) the corresponding sediment concentrations at z = 1.02 cab. The displayed time series are the first 200 s of data for case B. The individual waves selected according to the high concentration events are shown with the thick line (top panel). The circles in the bottom panel indicate peak concentrations that exceed the mean + standard deviation (dashed line).
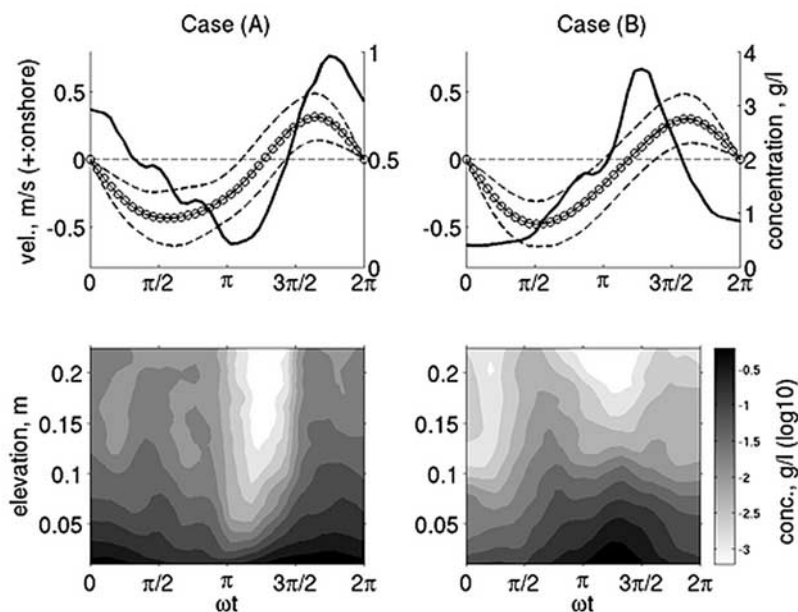
Figure 7. Ensemble-averaged horizontal velocities (circles), with ±1 standard deviation (dashed line), and vertically integrated suspended sediment concentration (SSC) (solid line, top panels), and the vertical distribution of the ensemble-averaged SSC (bottom panels). See color version of this figure in the HTML.

the ensemble average over all waves could smear out the sediment distribution pattern. Another ensemble averaging technique is to average by SSC "events" by picking significant suspension events from the whole record and ensemble averaging the concentration and flow after aligning the temporal peaks in SSC [*Dick et al.*, 1994]. The temporal variation in concentration can be seen clearly by this approach, but the relation with the wave phase is not as clearly seen, because the ensemble averaging is done according to elapsed time from the peak of each event, rather than according to wave phase. Here we use a new technique that selects significant SSC events but still ensemble averages by wave phase. SSC events are selected using the criterion that the peak SSC during the event exceeds the record mean concentration by at least 1 standard deviation. Then each SSC event is associated with the particular wave during which the concentration peak occurs. Ensemble averages of SSC and hydrodynamics are then calculated according to wave phase. This process selects the waves within a randomly varying wave record that are most responsible for the entrainment and suspension of sediment. It is particularly useful in identifying the correspondence between fluctuations in concentration and wave phase.

[22] Following this procedure, 102 wave-induced suspension events were selected out of a total of 344 waves for case A. For case B, 109 wave-induced suspension events were selected out of 367 waves. Examples of the selected waves for case B are shown in the top panel in Figure 6. In the bottom panel the corresponding peak concentrations are shown with circles. We have tested whether the use of zero down-crossings rather than zero up-crossings to select the waves has a significant effect, and we found that the results to be presented below are essentially unchanged.

[23] The selected waves and concentration events were then ensemble averaged by wave phase. In Figure 7 the ensemble average of the vertically integrated concentration as well as the ensemble average of horizontal velocity are shown in the top panels. The vertical structure of the ensemble average of the SSC is shown in the bottom panels of Figure 7. The concentration in the top panel is the result of the integration of the vertical distribution of concentration in the bottom panel, and it is drawn because the overall pattern of the suspended sediment concentrations can be easily compared with the horizontal velocity. In Figure 7, the velocity shown is the cross-shore component, and velocities have positive values when the flow is directed onshore.

[24] The ensemble-averaged velocities in Figure 7 have similar patterns in both case A and case B. Both of them show an asymmetry with higher maximum velocity in the offshore direction than in the onshore direction. This is due to the presence of offshore mean currents of approximately 6 to 8 cm/s. It should be noted that the strength of the mean currents of the whole time series is approximately the same as the mean of the time periods selected for ensemble averaging.

[25] Though the ensemble-averaged velocities show similar patterns for both cases, the distributions of the SSC are very different. In case A the concentration peak occurs near the time of maximum onshore velocity (well after the offshore to onshore flow reversal) and then the SSC decreases over the rest of the wave period. In case B the peak of the concentration occurs near the time of offshore to onshore flow reversal. The difference in the timing of the peak concentration is related to flow reversal, and may be understood by considering the SSC measurement location relative to the ripple crest location. As shown in Figure 3, the ABS was located about 10 cm shoreward of the ripple crest for case A, and about 30 cm seaward of the ripple crest for case B. If the sediment were entrained from the flank offshore of the ripple crest at the time of flow reversal by the action of the turbulent eddies, the sediment cloud would
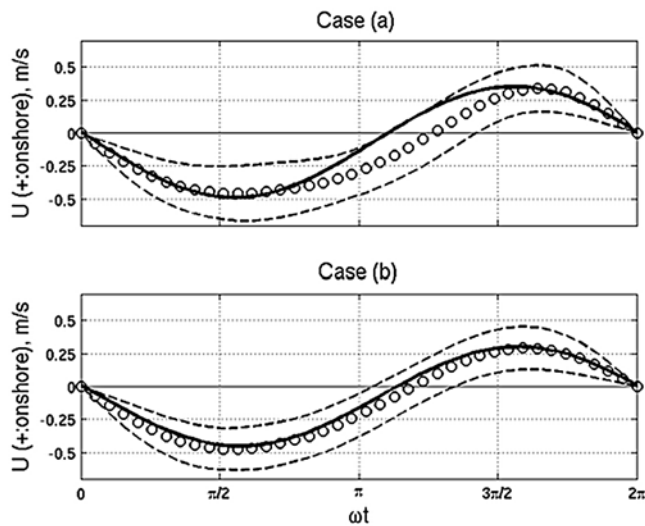
Figure 8. Horizontal velocity comparison over one wave period: circles, ensemble-averaged data and (dashed lines) ±1 standard deviation at P1 (case A) and P2 (case B); solid line, Dune2d calculations at P1 (case A) and P2 (case B).

subsequently be advected shoreward over the ripple by the flow. In case B the highest concentrations are measured near the time of offshore to onshore flow reversal (Figure 7). This is expected because the concentration measurements are located on the offshore flank of the bedform, where the sediment cloud is expected to form near the time of flow reversal. In contrast, the ABS for case A is located on the shoreward side of the ripple crest. If the sediment cloud were formed on the offshore flank of the ripple at the time of offshore to onshore flow reversal, this cloud would be carried by the onshore flow and would be detected by the ABS at a later time, which is consistent with Figure 7.

[26] In summary, the observations are consistent with the hypothesis that sediment is entrained on the offshore slope of the ripple, and that the cloud of suspended sediment begins to move upward and onshore at the time of the offshore-to-onshore velocity reversal. However, these data only provide a limited description for the suspension process. In order to provide a more detailed description of the turbulence and sediment dynamics, the numerical model is utilized in the next section.

[27] Before presenting the model results, we first illustrate how the model is driven by the measured velocities. The model is forced by the pressure gradient corresponding to a sine wave added to that corresponding to the mean current. In Figure 8, the model output horizontal velocities at the top of the domain for a typical model run are compared with the ensemble-averaged velocities from Figure 7. These show approximate agreement sufficient for the present studies. In future studies the model code will be modified so that the model can be forced by an arbitrary pressure gradient time series.

4.2. Model Predictions of the Temporal and Spatial Variations of the Flow, Turbulence, and Concentration

[28] One of the difficulties in the investigation of sediment suspension over rippled seabeds is the fact that

uniformity in the cross-ripple direction is not likely because of the irregular shape of the bottom. The temporal and spatial variations of the bottom shear stresses are not easily predictable, due to the complexity of the flow and turbulence over the ripples. Without fully 2-D or 3-D measurements of hydrodynamics and SSC, a model is extremely useful to fill in the missing data space, as will be seen.

[29] In order to understand the behavior of the suspended sediment above ripples, it will first be helpful to review sediment suspension due to oscillatory flow above a flat bed using the Dune2d model. It is generally assumed that the reference concentration that serves as bottom boundary condition for suspended sediment is directly related to the local shear stresses. The reference concentration increases as the shear stress increases, which is approximately proportional to the velocity squared. An example of the suspended sediment concentration distribution over a flat bed predicted by Dune2d is shown in Figure 9. The concentration and TKE are large at the same phase as the peak velocity magnitude near the bed, showing two peaks over one wave period. In this example the pressure gradient used as the input forcing is approximately the same as observed in the field for case A, showing asymmetry in the magnitude of maximum velocity in onshore and offshore flow. The magnitudes of both the concentration and the TKE show the asymmetry between onshore and offshore phase. This indicates that the sediment concentration and TKE are directly influenced by the velocity magnitude. Once sediment is entrained from the bed, it is diffused upward in a smooth manner, showing phase differences in the vertical direction.

[30] In contrast to flat seabeds, the flow above rippled seabeds has temporal and spatial variations that are strongly influenced by the turbulent vortices that may be generated in the lee of ripple crests. The entrainment, mixing, and transport of SSC will also be influenced by the vortices. Figure 10 shows the model-predicted flow at four different times for the bedform profile of case A. At t_1 the offshore flow has its maximum magnitude, and t_2 is the time of offshore to onshore flow reversal. At t_3, the onshore flow has its maximum velocity, and t_4 is the time of onshore to offshore flow reversal. A vortex structure is formed on the offshore side of the ripple crest at time t_2 (Figure 10b). Since the time t_2 is just before the offshore to onshore flow reversal, the flow outside the boundary layer is weakly directed offshore, but there are strong flows directed onshore near the bed due to the velocity phase lead inside the boundary layer. The strong vertical gradient of the horizontal velocity results in the vortex generation at this time.

[31] However, no vortices are formed at the time of onshore to offshore flow reversal, t_4. One explanation for this is the asymmetry in the magnitude of the horizontal velocity. Because the maximum offshore horizontal velocity is larger than the maximum onshore velocity outside boundary layer (P1), the maximum velocity magnitude as well as the vertical gradient is also larger inside the bottom boundary layer at the time of offshore to onshore flow reversal (t_2). The horizontal velocity profiles can be compared at the time of offshore to onshore flow reversal (t_2) and at the time of onshore to offshore flow reversal (t_4). The magnitude of the onshore velocities at t_2 is about 30 cm/s near the bottom, while the magnitude of the offshore
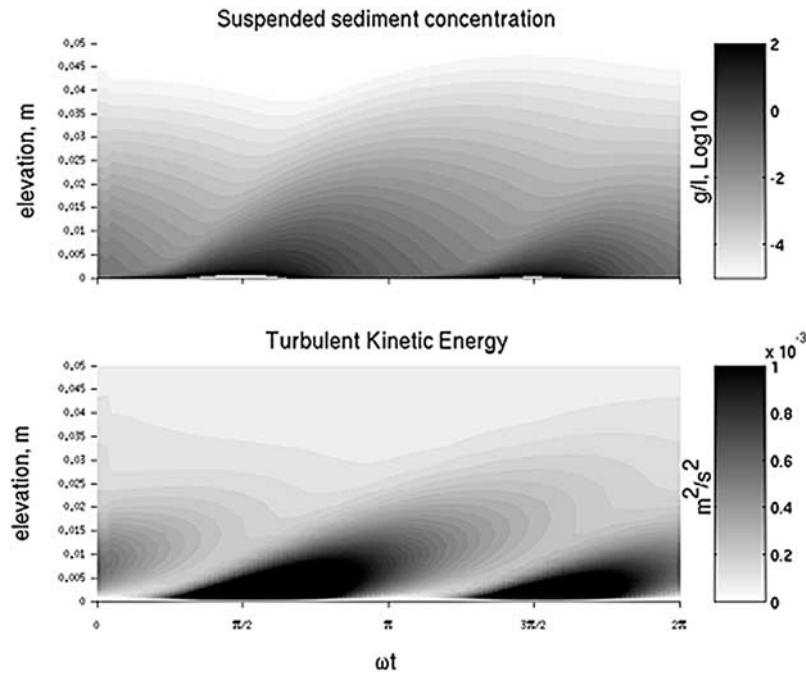
Figure 9. Time variation of SSC and turbulent kinetic energy (TKE) over flat bed predicted by Dune2d. See color version of this figure in the HTML.

velocity at t_4 is about 20 cm/s. The corresponding vertical gradient of the horizontal velocity is also higher at time, t_2. Thus the smaller velocity magnitude and the smaller vertical gradient do not generate vortices at time t_4. At the time of maximum onshore and offshore velocities (t_1 and t_3), the

flows are parallel to the bottom topography, showing no sign of flow separation. At these wave phases, the vertical gradients of the flows are small.

[32] The bedforms and hydrodynamics of case B are compared at the same time steps (t_1, t_2, t_3, and t_4) in
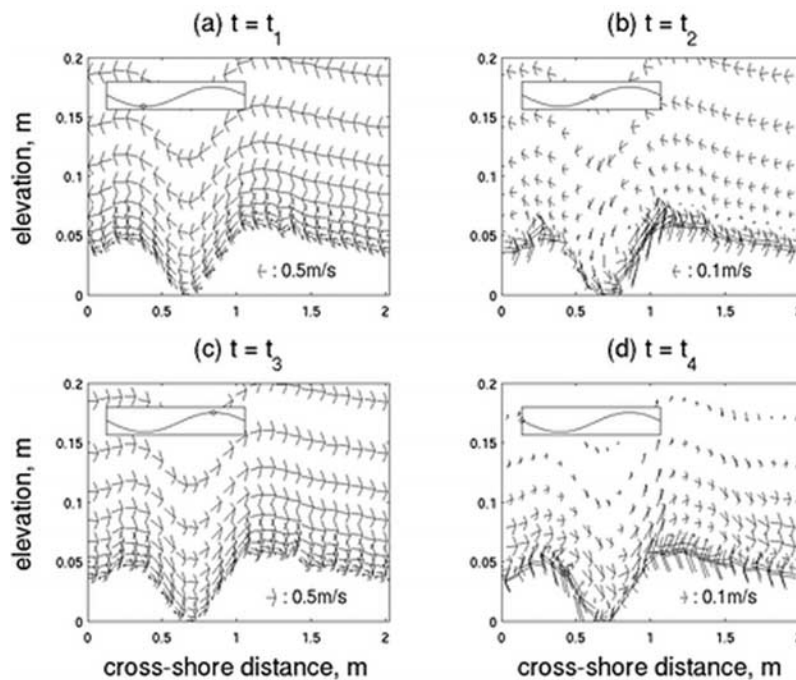
Figure 10. Time variation of velocity field, case A: t_1, time of maximum offshore velocity; t_2, time of offshore-onshore flow reversal; t_3, time of maximum onshore velocity; t_4, time of onshore-offshore flow reversal. Note that the arrow scale in Figures 10b and 10d is larger than that of Figures 10a and 10c.
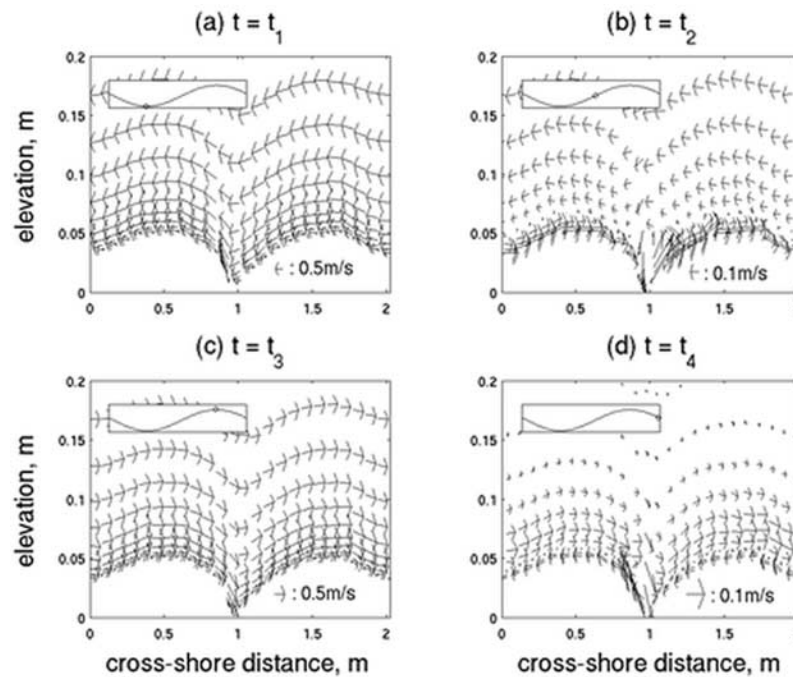
Figure 11. Time variation of velocity field, case B: t_1, time of maximum offshore velocity; t_2, time of offshore-onshore flow reversal; t_3, time of maximum onshore velocity; t_4, time of onshore-offshore flow reversal.

Figure 11, in which the velocity distributions are similar to case A. The vertical gradients are higher at t_2 than t_4, and the flows are parallel to the bottom at strong wave phases, t_1 and t_3.

[33] The temporal and spatial variations of the TKE and suspended sediment concentration are shown in Figures 12 and 13. The left four panels in Figure 12 are the TKE variations for case A, and the right four panels are for case B. The time t_1, t_2, t_3, and t_4 are identical to the times in Figures 10 and 11. At the offshore to onshore flow reversal (t_2), high values of TKE are found near the seabed, and the highest TKE is concentrated on the offshore side of ripple crest, which is consistent with the location of the vortex. The high TKE is indicative of the large velocity fluctuations due to the vortex. At the time of strong onshore velocity, t_3, high TKE is observed near the ripple crest. This is because the high TKE generated by the vortex at t_2 is advected horizontally with the onshore flow. At the time of onshore to offshore flow reversal (t_4), this high TKE is advected farther in the onshore direction. Also, the TKE along the ripples is smaller at t_4 than t_2 because of the wave asymmetry.

[34] The variations of the SSC are similar to the TKE variations as shown in Figure 13. A cloud of sediment is observed at the offshore slope of the ripple crest at time t_2. This sediment cloud indicates that the sediments are entrained from the seabed due to the vortex. This entrained sediment cloud is advected horizontally with the flow to a position near the ripple crest at t_3 and even farther at t_4. The cloud is enlarged and diluted due to diffusion.

[35] At the time of maximum offshore flow (t_1), high concentrations are also found along the bed. This is due to the reference concentration boundary condition formulation in Dune2d. The concentration near the bed is high at large

velocities just as in the case of a flat bed (Figure 9). Dune2d is formulated to describe the entrainment from the bed at strong bed shear stresses, and the subsequent mixing by turbulent diffusion. The entrainment of the sediments due to the turbulent vortex at the time of flow reversal can also be described in this context. The strong near-bed velocities due to the phase lead inside the bottom boundary layer entrain the sediment from the bed into the turbulent vortex at the time of flow reversal. Then the sediment is advected with the flow and diffused by turbulent gradient diffusion until sediment settles down to the bed due to gravity.

4.3. Comparison of the Model Predictions With Data

[36] The numerical calculations from Dune2d are next compared with the ensemble-averaged field measurements. This sort of comparison should be considered as quantitative but not strict. The field measurements have been ensemble averaged as described earlier, and the model is forced by a combined mean current and oscillatory flow, in order to approximate the ensemble-averaged velocity. The comparison of the horizontal velocities at the positions P1 and P2, shown previously in Figure 8, show reasonable agreements with data. However, the comparison is not between true realizations, which would exhibit greater variability. Rather, the comparison should be considered as between a typical suspension event in the field and the corresponding model predictions. It remains as future work to force the model in a true time-dependent fashion, and to address the issue of stochastic forcing in the natural system.

[37] The ensemble averages of the TKE measurements are compared with Dune2d predictions in Figure 14. The estimation of the turbulence from velocity measurements is performed according to the method suggested by
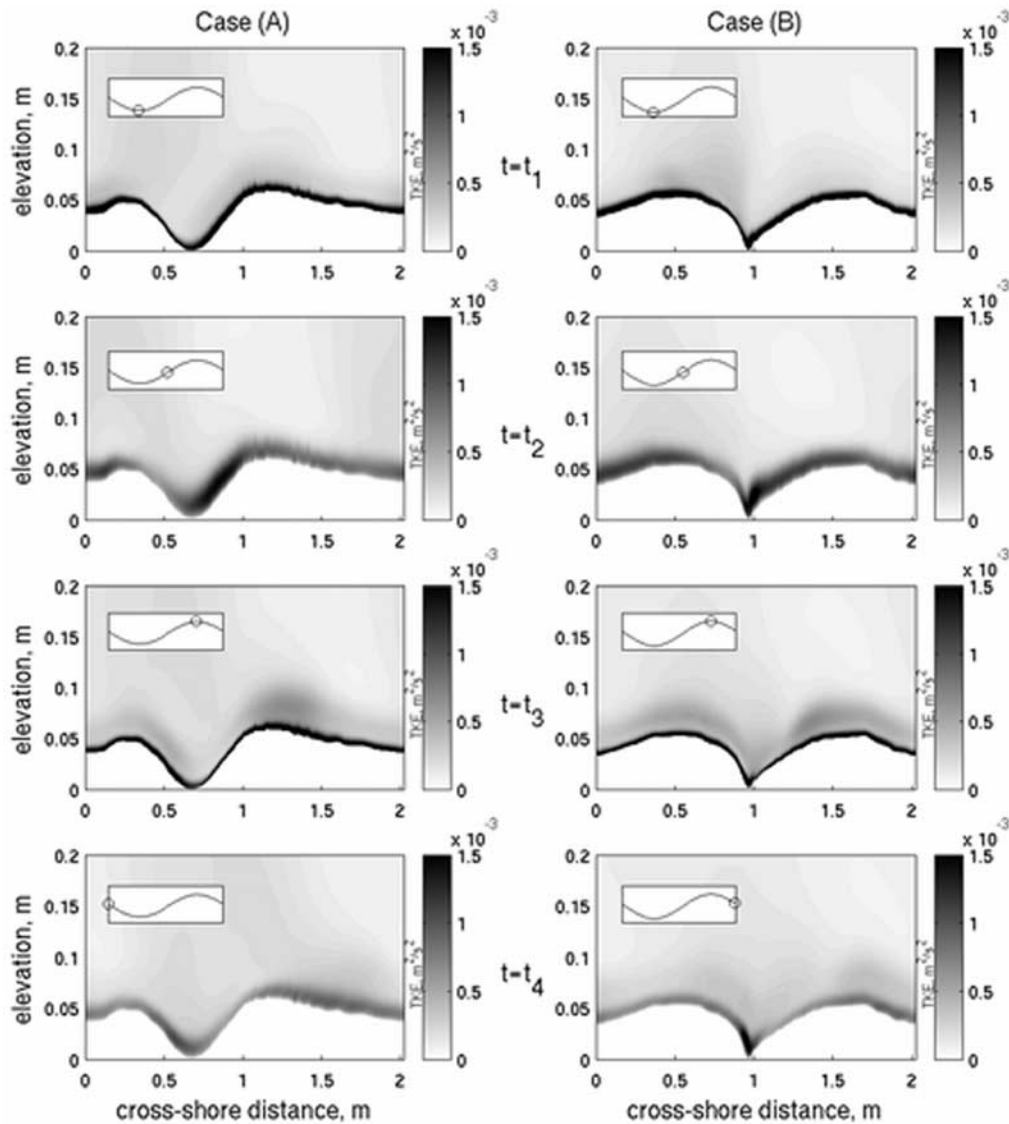
Figure 12. Temporal and spatial variations of the distributions of the turbulent kinetic energy (m²/s²); t_1, t_2, t_3, and t_4 are the same as in Figures 10 and 11. See color version of this figure in the HTML.

Trowbridge [1998], which separates the wave motion from turbulent velocity fluctuations. In Figure 14, the measured TKE (circles) and model predictions (solid line) are compared over one wave period at the position P1 (case A) and P2 (case B), which are approximately 20 cm above the seabed. The measured TKE is 2 to 3 times larger than the model predictions, and the measurements indicate a relatively stronger variation in time over a wave cycle. We will return to this discrepancy later, in section 5.

[38] Next we compare the measured SSC to the model predictions. The data and numerical calculations at P1 are compared in Figure 15 for case A. In Figure 15a, the ensemble-averaged SSC shows that a concentration peak is found near the time of $3\pi/2$, and this peak lasts for more than half of the wave cycle. The timing of this peak in concentration is not consistent with sediment suspension above a flat bed because the peak is not at the time of the peak velocity. The SSC peak can be explained if the sediment cloud is advected horizontally toward and through

the measurement location. In Figure 15b, the calculated SSC also has one peak near the time of $3\pi/2$. In Figure 13, it is observed that the sediment cloud suspended at time t_2 moves through the ABS location near the time of $3\pi/2$ (t_3). Thus the concentration peak in Figure 15b is the sediment cloud that is transported from the offshore side of the ripple crest, after it was suspended at the time of offshore to onshore flow reversal. Since the times of the concentration peak between the field measurements and model predictions are in agreement, it can be concluded that the distribution of the SSC shown in Figure 15 results from the advection of the sediment cloud that was suspended by turbulent vortex.

[39] Figure 16 shows the time variation of the measured and predicted SSC for case B. The concentration measurements are located on the offshore slope of the ripple crest. High sediment concentrations occur near the time of offshore to onshore flow reversal in both the measurements and the model predictions. However, the times of the peak concentrations are slightly different. The measured peak
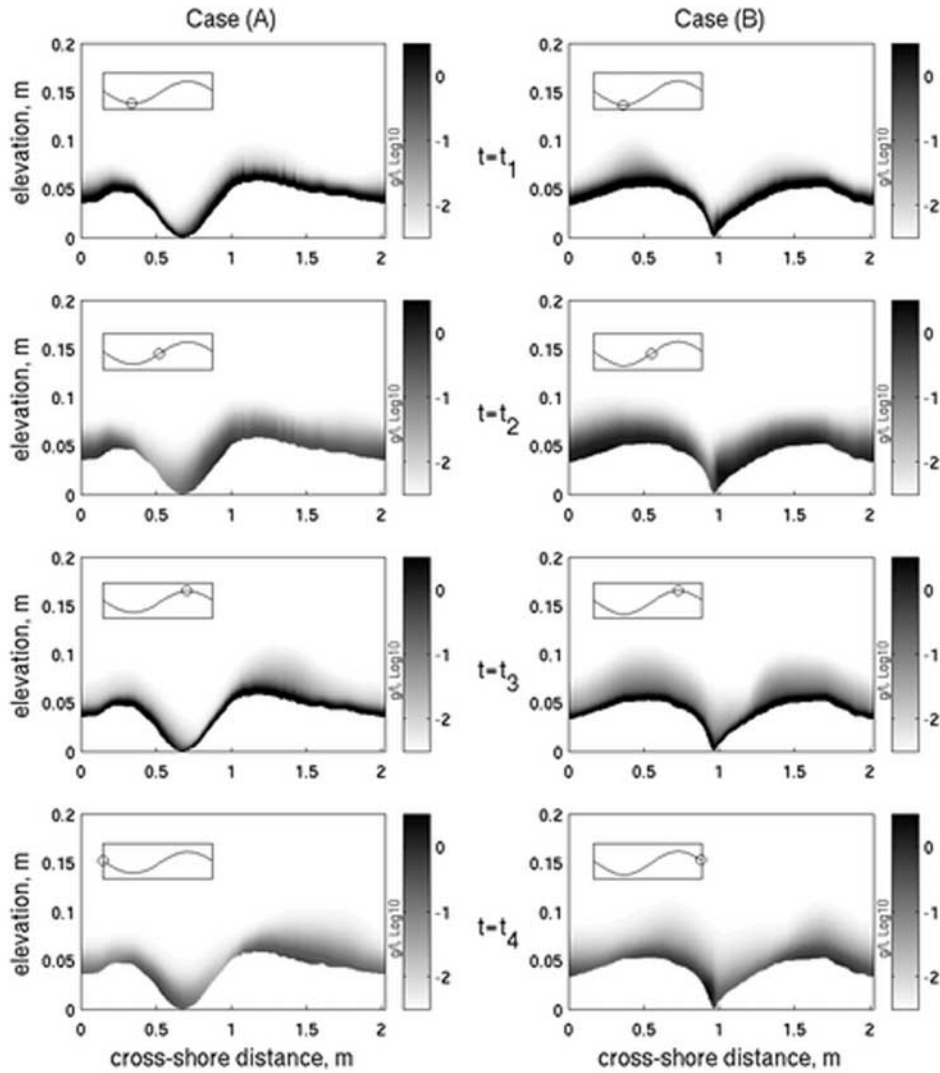
Figure 13. Temporal and spatial variations of the distributions of the SSC (Log10(g/L)); t_1, t_2, t_3, and t_4 are the same as in Figures 10 and 11. See color version of this figure in the HTML.

concentration occurs at approximately $5\pi/4$, but the peak model prediction occurs at approximately $3\pi/4$. The use of the reference concentration in Dune2d may explain this discrepancy. Since the turbulent vortex is formed and starts to entrain sediment from the bed at the time of flow reversal, a sediment cloud is formed at (or slightly after) the flow reversal. However, Dune2d predicts high reference concentrations coincident with high velocities.

[40] There is a significant discrepancy between the magnitude of the observed SSC and the model predictions elevations higher than a few centimeters above the seabed. For example, the sediment cloud shown in Figure 15b is suspended only up to 5 cab and exists only for a short time; the measured SSC in Figure 15a extends higher than 10 cab, and lasts longer. In order to investigate the discrepancies in the magnitude of SSC, a comparison of the measured and modeled profiles of the time mean SSC are shown in Figure 17. Recall that the magnitudes of the sediment concentration near bottom (about 1 cab) are comparable between data and model, and that a bed roughness of $10.5d_{50} - 14.0d_{50}$ has been imposed in order to achieve

this agreement. Figure 17 shows that the model prediction of SSC is significantly lower compared to the measured values as the elevation increases above 1 or 2 cm.

5. Discussion

[41] Both field observations and numerical simulations indicate that turbulent vortices are generated at the offshore side of the LWR crest at the time of the flow reversal. The turbulent kinetic energy and the SSC patterns show that high turbulent energy and high concentrations are found near the location of the turbulent eddies, which indicates that the eddies form sediment clouds. Moreover, these sediment clouds are advected with the flow as they diffuse. Both the field observations and the model calculations basically support the hypothesis that sediment is entrained into suspension by a vortex-like separated flow structure that occurs on the offshore flank of the LWR near the time of flow reversal.

[42] However, no vortices are generated at the time of the onshore to offshore flow reversal. There are a few potential
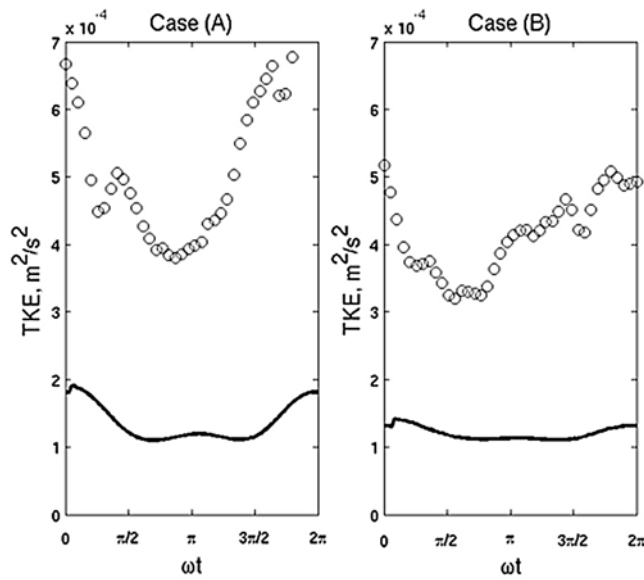
Figure 14. Comparison of TKE between data and model predictions at P1 and P2: solid line, model predictions; circles, measured data.

explanations for this phenomenon. One explanation for this is the asymmetric nature of the near-bed velocities that result from the combination of waves and mean currents. The magnitude of the maximum offshore velocity is greater than the maximum onshore velocity, and the duration of the offshore velocity is longer than the duration of the onshore velocity. A second explanation, which is probably related to the previous explanation, is that the asymmetry in the bedform shape leads to greater flow separation during the offshore motion. In order to investigate these possible

explanations for the asymmetry, we have conducted additional simulations in which the mean flow is set to zero, but the same oscillatory forcing is applied over the same bedforms. The results of this test, shown in Figure 18, suggest that without the presence of a mean current the suspension process is more symmetric; however there is still some level of asymmetry due to the ripple shape. The relative effects of wave period, velocity skewness and asymmetry, mean currents, and ripple shape should be explored further in the future.

[43] The comparison between model predictions and field observations reveals some obvious discrepancies. The magnitudes of the SSC are under-estimated by Dune2d at high elevations, even though the modeled SSC near the seabed is forced to be similar to the measured SSC through the adjustment of the bed roughness. The TKE is also underestimated by the model in comparison to the measurements. We do not know conclusively the sources of these discrepancies; the following provides some possible explanations.

[44] One possible explanation why the model has underestimated the SSC and TKE above the bed is the uncertainly regarding the parameterization of the seabed roughness. Because the bed surface of the computational domain is smooth, the effects of the small-scale eddies that are formed near the real boundary due to rough beds are not directly incorporated in the simulations. Rather, they are parameterized by the hydraulic roughness. In order to examine the effects of bed roughness more effectively, we superimposed 20 SWR [*Hanes et al.*, 2001] upon the LWR in the computational domain. The size of each SWR is 10 cm in length and 0.5 cm in height. In order to adequately resolve the motions of small-scale eddies due to the SWR, the grid resolution had to be finer than the original grid system of 120×60 grid points. *Andersen* [1999] pointed out that the
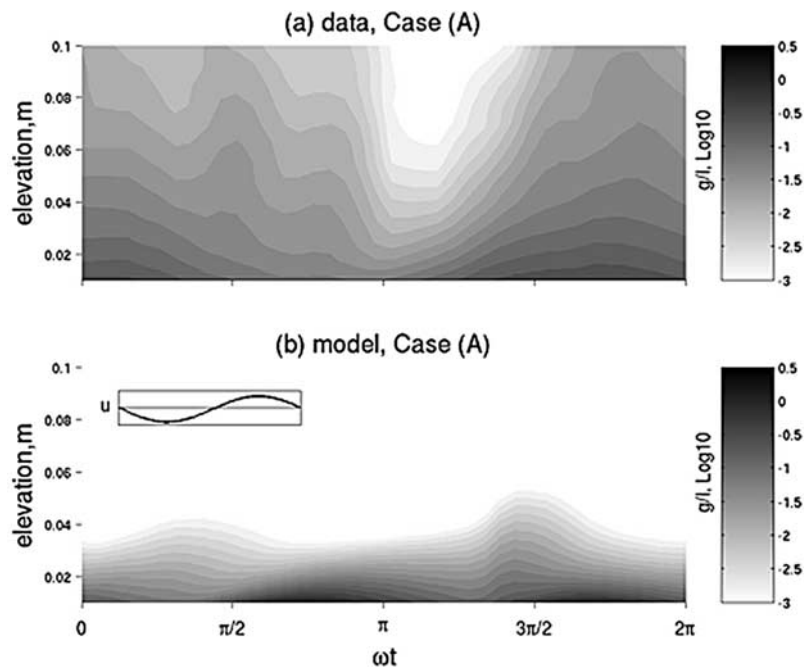
Figure 15. Comparison of the vertical distribution of the suspended sediment concentration between data and model results at P2 for case (A). See color version of this figure in the HTML.
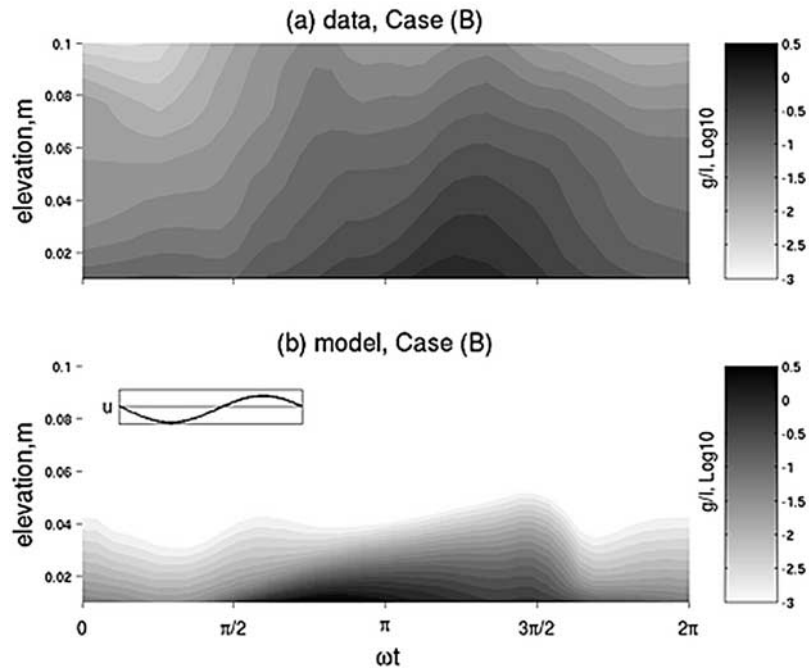
Figure 16. Comparison of the vertical distribution of the suspended sediment concentration between data and model results at P2 for case (B). See color version of this figure in the HTML.

model is stable if the horizontal grid spacing is small compared to the orbital diameter, $\Delta x/a < 0.012$, and also small compared to the ripple wavelength. The vertical grid spacing should be sufficiently fine that the first grid cell is contained inside the viscous sublayer. To meet these conditions for the simulations including SWR we generated 400×100 grid points, so $\Delta x/a \approx 0.0118$ and $y^+ \approx 2.5$ for the first cell. Possible side effects related to insufficient grid resolution used in these particular simulations are presented in Appendix A.

[45] The mean SSC profile resulting from these higher-resolution simulations (that include SWR) is shown in Figure 19 along with other profiles for case A. The effect of including the SWR is obvious; the new hydraulic roughness required to match the SSC with the measurements at the lowest elevation (1.17 cm) has been reduced to $6.0d_{50}$ from the original value of $10.5d_{50}$. Also, the slope of SSC profile becomes a bit higher than the slope of the original SSC profile (without SWR), so it is concluded that the vertical mixing is somewhat enhanced due to the increased bed roughness. However, the discrepancy from the measured data is still significant and cannot be explained by the inclusion of SWR and a finer-resolution grid.

[46] Another contributing factor to the underestimation of the SSC by Dune2d may be a consequence of using a rigid lid at the top of the relatively shallow computational domain. The use of a rigid lid confines the flow to be horizontal at the upper surface. This certainly eliminates the vertical velocities induced by the surface gravity waves and also may inhibit turbulent vertical fluctuations. Figure 20 shows the comparison between measurements and model predictions of the vertical velocity. The magnitude of the vertical velocity calculated by Dune2d is much less than

that of the measurements, even though the magnitude of horizontal velocity is in agreement with measurements. However, in defense of the model and the rigid lid assumption, we point out that the model has been used quite successfully in a number of applications similar to this study [*Andersen*, 1999; *Fredsoe et al.*, 1999; *Jensen and Fredsoe*, 2001]. A third contributing factor for the discrepancy for the SSC profile is that the gradient diffusion
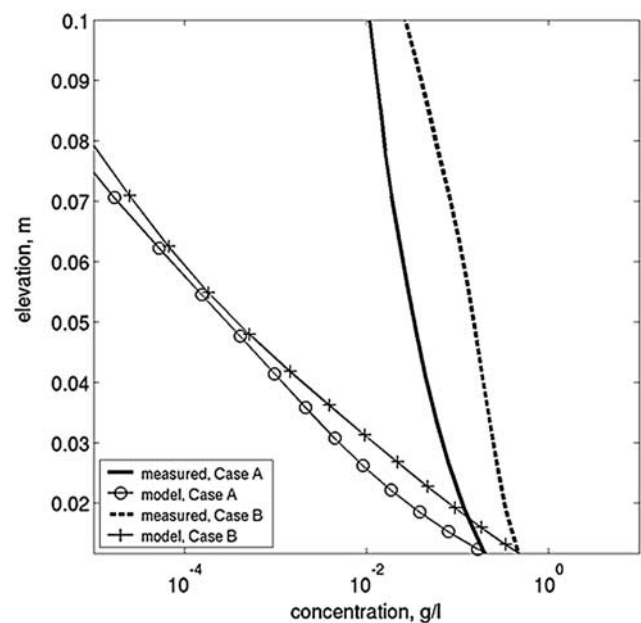
Figure 17. Comparison between measurements and model predictions of profiles of time-averaged SSC.
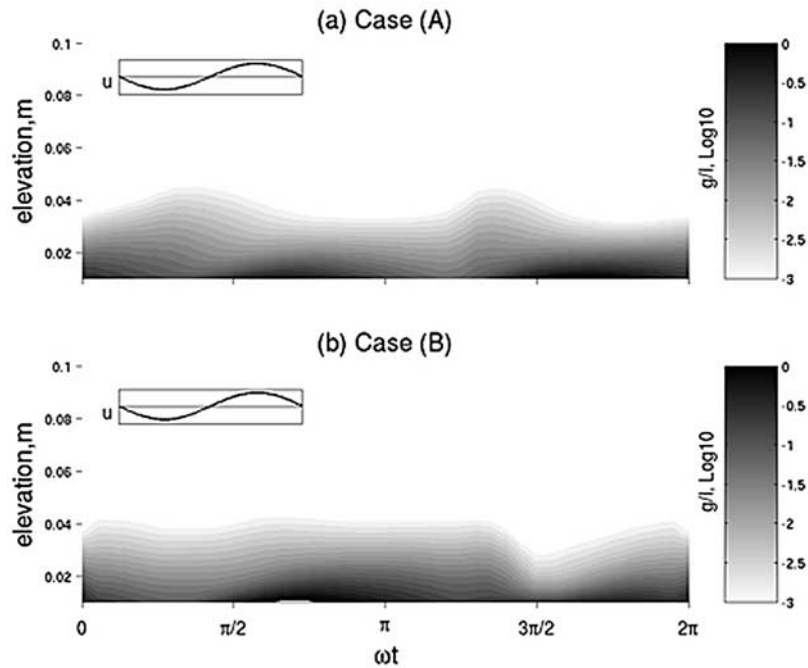
Figure 18. SSC for bed forms of case A and case B using the measured ensemble oscillatory forcing, but with the mean current removed. Compare to Figures 15b and 16b. See color version of this figure in the HTML.

contribution to the vertical flux of the sediment, given in equation (5), is underestimated in the model.

$$(W - w_s)C + \nu_t \frac{\partial C}{\partial z}. \tag{5}$$

[47] In equation (5) the vertical sediment flux is determined by the balance between the settling velocity, convection by the mean vertical velocity, W, and gradient diffusion.
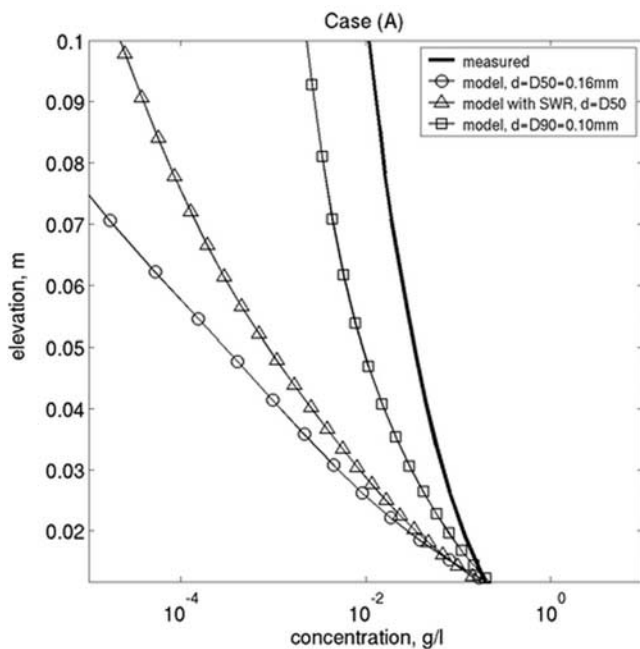
Figure 19. Comparison of mean SSC profiles with different numerical conditions, case A: solid line, measured data; circles, model predictions with $d = d_{50}$ and without SWR (original coarse grids); triangles, model predictions with $d = d_{50}$ but with SWR (fine grids); squares, model predictions with fine sediments ($d = d_{90}$) without SWR (original coarse grids).
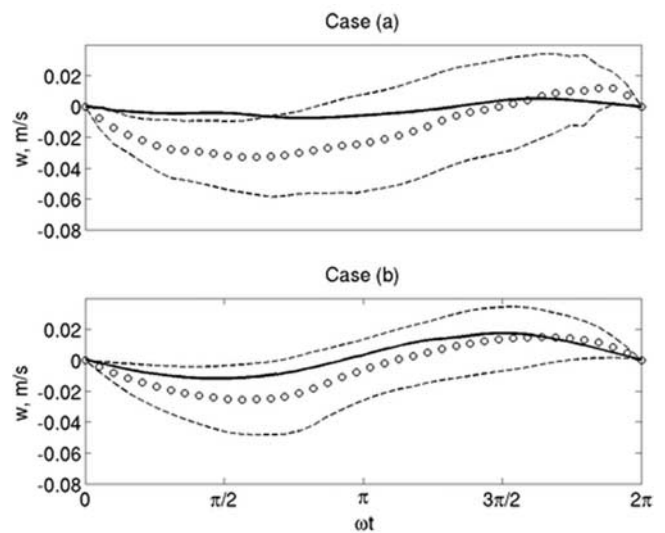
Figure 20. Vertical velocity comparison over one wave period: circles, ensemble-averaged data with ±1 standard deviation (dashed lines) at P1 (case A) and P2 (case B); solid line, Dune2d calculations at P1 (case A) and P2 (case B).
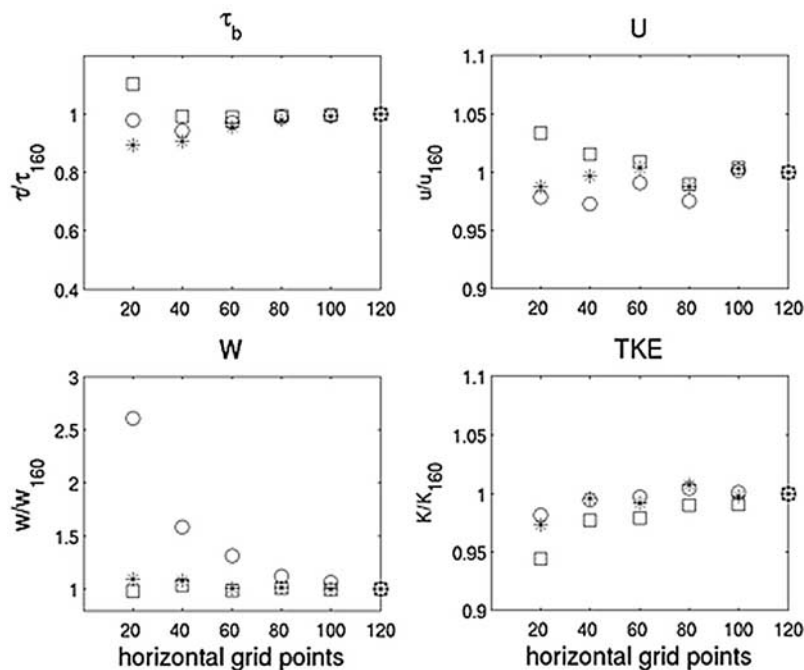
Figure A1. Comparison of the flow properties computed at different grid resolutions, normalized by the values at the finest resolution (160×80): circles, $x = 5$ cm, $z = 0.11$ cab; crosses, $x = 3.5$ cm, $z = 0.0.35$ cab; squares, $x = 6.5$ cm, $z = 0.0.35$ cab (except for τ_b).

As seen previously in Figure 14, the TKE predicted by Dune2d is lower than the measured values by a factor of 2 to 3. It can be assumed that the Reynolds stress, $\overline{-u'w'}$, is also low, in a manner similar to the TKE. If the Reynolds stress is low, then the eddy viscosity (i.e., the eddy diffusivity) will also be underestimated.

[48] A relatively simple way to examine the effects of the underestimation of the sediment flux without modifying the numerical code of Dune2d is to change the value of the settling velocity. By decreasing the settling velocity, w_s, the total flux increases. In Figure 20, the SSC profile with decreased w_s is also plotted, where the d_{90} (0.10 mm) was employed for the sediment diameter instead of d_{50} (0.16 mm). The slope of the SSC profile for the finer sediment is indeed much steeper, and it is in fact similar to the measurements. We note here that it is also possible that the suspended sediment size in the field was significantly finer than the bed sediment. Although even if this were the case, and the modeled and measured SSC profiles agreed well with each other, the model is still underpredicting the TKE and vertical velocities.

[49] Finally, we mention that a limitation of the present study is that these investigations assume two-dimensionality in the vertical and cross-shore direction. However, 3-D bedforms often exist in nearshore areas. The flow and the SSC will be more complicated over 3-D structures. Therefore there is a need to develop instrumentation for fully 3-D measurements. There is a corresponding need for fully 3-D simulations operating at realistic spatial scales and flow velocities.

Appendix A: Grid Resolution Considerations

[50] The selection of model grid scales for the cases in which SWR were superimposed upon the larger bedforms

was unusually demanding because of the need to resolve the smaller-scale bedforms while still covering the domain of the larger bedforms without making the computational demands too great for our computer and patience. On the basis of a series of sensitivity tests, we chose a grid resolution that resulted in approximately 22 horizontal and 20 vertical grid points per SWR. Because adding the SWR to the simulation had the effect of increasing the SSC and reducing the discrepancy between the model and the observations, it is desirable to confirm that the grid size employed was sufficient, and that increased resolution would not significantly change the results.

[51] In order to explore the possible influence of the grid size upon the results, we have conducted additional simulations of oscillatory flow above a SWR. The SWR has the same shape and size as previously, in a computational domain of length 0.1 m and height 0.25 m, forced by oscillatory flow similar to case 1. A series of grid sizes were used: 22×20 (closest to the case in paper), 42×20, 62×30, 82×40, 122×60, and 160×80.

[52] In Figure A1, we show the sensitivity of four modeled flow properties to the grid size: bottom shear stresses (τ_b), horizontal velocity (u), vertical velocity (w), and turbulent kinetic energy (TKE). These are compared at three horizontal locations of $x = 3.5$, 5.0, and 6.5 cm. The vertical locations for u, w, and TKE are from 0.11 cab (for $x = 5$ cm) to 0.35 cab (for $x = 3.5$ and 6.5 cm).

[53] The comparisons are made at the time of maximum flow, when the differences due to grid size are expected to be largest. Figure A1 shows that the differences due to grid size are not significant for most of the flow properties. Except for the vertical velocity at $x = 5.0$ cm (the ripple crest), the differences between the coarsest and finest grid resolutions for all the other quantities are within approxi-

mately 5 to 10%. The error in the vertical velocity at the ripple crest for the coarsest grid is significant; however, it is important to note that the vertical velocity is overestimated using the coarsest grids, so that correction of this effect would not improve the discrepancy between the modeled and measured SSC. We conclude that small errors result from employing only 22×40 grid points per SWR, and this effect is small compared to the discrepancies between the model and the observations that were discussed earlier.

References

Andersen, K. H. (1999), The dynamics of ripples beneath surface waves and topics in shell models of turbulence, Ph.D. dissertation, Tech. Univ. of Denmark, Lyngby, Denmark.

Bagnold, R. A. (1946), Motion of waves in shallow water: Interaction between waves and sand bottoms, *Proc. R. Soc. London, Ser. A, 187*, 1–15.

Barr, B. C., D. N. Slinn, T. Pierro, and K. B. Winters (2004), Numerical simulation of turbulent, oscillatory flow over sand ripples, *J. Geophys. Res., 109*, doi:10.1029/2002JC001709, in press.

Black, K. P., P. D. Osborne, M. O. Green, and P. V. Villard (1997), Intra-wave suspended sediment concentrations over bedforms, paper presented at Combined Australasian Coastal Engineering and Ports Conference, Cent. for Adv. Eng., Christchurch, New Zealand.

Brenninkmeyer, B. M. (1976), In situ measurements of rapidly fluctuating, high sediment concentrations, *Mar. Geol., 20*, 117–128.

Dick, J. E., M. R. Erdman, and D. M. Hanes (1994), Suspended sand concentration events due to shoaled waves over a flat bed, *Mar. Geol., 119*, 67–73.

Engelund, F., and J. Fredsoe (1976), A sediment transport model for straight alluvial channels, *Nord. Hydrol., 7*, 293–306.

Fredsoe, J., O. H. Andersen, and S. Silberg (1985), Distribution of suspended sediment in large waves, *J. Waterw. Port Coastal Ocean Eng., 111*(6), 1041–1059.

Fredsoe, J., K. Andersen, and B. M. Sumer (1999), Wave plus current over a ripple-covered bed, *Coastal Eng., 38*, 177–221.

Grant, W. D., and O. S. Madsen (1979), Combined wave and current interaction with a rough bottom, *J. Geophys. Res., 84*(C4), 1797–1808.

Hanes, D. M. (1988), Intermittent sediment suspension and its implication to sand tracer dispersal in wave-dominated environments, *Mar. Geol., 81*, 175–183.

Hanes, D. M. (1991), Suspension of sand due to wave groups, *J. Geophys. Res., 96*(C5), 8911–8915.

Hanes, D. M., E. D. Thosteson, Y. S. Chang, C. Conner, and C. E. Vincent (1998), Field observations of small scale sedimentation process, 26th International Conference on Coastal Engineering, Am. Soc. of Civ. Eng., Copenhagen, Denmark.

Hanes, D. M., V. Alymov, Y. S. Chang, and C. D. Jette (2001), Wave formed sand ripples at Duck, North Carolina, *J. Geophys. Res., 106*(C10), 22,575–22,592.

Hansen, E. A., J. Fredsoe, and R. Deigaard (1994), Distribution of suspended sediment over wave-generated ripples, *J. Waterw. Port Coastal Ocean Eng., 120*(1), 37–55.

Hay, A. E., and A. J. Bowen (1994), Coherence scales of wave-induced suspended sand concentration fluctuations, *J. Geophys. Res., 99*(C6), 12,749–12,765.

Jensen, B. L., and J. Fredsoe (2001), Sediment transport and backfilling of trenches in oscillatory flow, *J. Waterw. Port Coastal Ocean Eng., 127*(5), 272–281.

Jette, C. D., and D. M. Hanes (1997), High resolution sea-bed imaging: An acoustic multiple transducer array, *Meas. Sci. Technol., 8*, 787–792.

Lee, T. H., and D. M. Hanes (1995), Direct inversion method to measure the concentration profile of suspended particles using backscattered sound, *J. Geophys. Res., 100*(C2), 2649–2657.

Lee, T. H., and D. M. Hanes (1996), Comparison of field observations of the vertical distribution of suspended sand and its prediction by model, *J. Geophys. Res., 101*(C2), 3561–3572.

Nielsen, P. (1988), Three simple models of wave sediment transport, *Coastal Eng., 12*, 43–62.

Nielsen, P. (1991), Combined convection and diffusion: A new framework for suspended sediment modeling, paper presented at Coastal Sediments '91, Am. Soc. of Civ. Eng., Seattle, Wash.

Nielsen, P. (1992a), *Coastal Bottom Boundary Layers and Sediment Transport*, World Sci., River Edge, N.J.

Nielsen, P. (1992b), Combined convection diffusion modeling of sediment entrainment, paper presented at 23rd International Conference on Coastal Engineering, Am. Soc. of Civ. Eng., Venice, Italy.

Osborne, P. D., and C. E. Vincent (1996), Vertical and horizontal structure in suspended sand concentrations and wave-induced fluxes over bedforms, *Mar. Geol., 131*, 195–208.

Patankar, S. V. (1980), *Numerical Heat Transfer and Fluid Flow*, Taylor and Francis, Philadelphia, Pa.

Sleath, J. F. A. (1982), The suspension of sand by waves, *J. Hydraul. Res., 20*(5), 439–452.

Thorne, P. D., and D. M. Hanes (2002), A review of acoustic methods for the study of small scale sediment transport processes, *Cont. Shelf Res., 22*, 603–632.

Thornton, E. B., and W. D. Morris (1978), Suspended sediments measured within the surf zone, paper presented at Coastal Sediments '77, Am. Soc. of Civ. Eng., New York.

Thosteson, E. D., and D. M. Hanes (1998), A simplified method for determining sediment size and concentration from multiple frequency acoustic backscatter measurements, *J. Acoust. Soc. Am., 104*(2), 820–830.

Tjerry, S. (1995), Morphological calculations of dunes in alluvial rivers, Ph.D. thesis, Tech. Univ. of Denmark (ISVA), Lyngby, Denmark.

Trowbridge, J. H. (1998), On a technique for measurement of turbulent shear stress in the presence of surface waves, *J. Atmos. Oceanic Technol., 15*, 290–298.

Vincent, C. E., D. M. Hanes, and A. J. Bowen (1991), Acoustic measurements of suspended sand on the shoreface and the control of concentration by bed roughness, *Mar. Geol., 96*, 1–18.

Vincent, C. E., S. W. Marsh, M. P. Webb, and P. D. Osborne (1999), Spatial and temporal structures of suspension and transport over megaripples on the shore face, *J. Geophys. Res., 104*(C5), 11,215–11,224.

Wikramanayake, P. N. (1993), Velocity profiles and suspended sediment transport, Ph.D. dissertation, Dep. of Civ. and Environ. Eng., Mass. Inst. of Technol., Cambridge.

Wilcox, D. C. (1998), *Turbulence Modeling for CFD*, second ed., DWC Ind., La Canada, Calif.

Zijlema, M. (1996), On the construction of a third-order accurate monotone convection scheme with application to turbulent flows in general domains, *Int. J. Numer. Methods Fluids, 22*, 619–641.

————————————

Y. S. Chang, Meteorology and Physical Oceanography, Rosenstiel School of Marine and Atmospheric Science, University of Miami, 4600 Rickenbacker Causeway, Miami, FL 33149, USA. (yschang@rsmas.miami.edu)

D. M. Hanes, Coastal and Marine Geology, U.S. Geological Survey Pacific Science Center, 400 Natural Bridges Drive, Santa Cruz, CA 95060, USA. (dhanes@usgs.gov)